PNAS RESEARCH ARTICLE | EARTH, ATMOSPHERIC, AND PLANETARY SCIENCES OPEN ACCESS

Tectonism rather than "snowball Earth" glaciation is responsible for the Great Unconformity

Rong-Ruo Zhan[a,b], Liang Duan[a,1], Massimiliano Zattin[b], Nicholas Christie-Blick[c], Bo Wan[d], Rong-Hao Wei[a], Zhao Yang[a], Jianqiang Wang[a], Longlong Gou[a], Valerio Olivetti[b], Kai-Yun Chen[a], and Xingliang Zhang[a,e]

Edited by Shuhai Xiao, Virginia Polytechnic Institute and State University, Blacksburg, VA; received September 1, 2025; accepted January 20, 2026

The Great Unconformity (GUn)—a widely recognized discontinuity and associated gap in the rock record between Precambrian and Cambrian rocks—represents a globally important interval of continental exposure and erosion that is notable also for the first appearance of all major animal phyla on Earth. However, its origin remains the subject of vigorous debate. Here, we present field relationships, and zircon and monazite U–Pb, biotite and muscovite Rb–Sr, and zircon (U–Th)/He thermochronology data for Precambrian crystalline basement rocks from North China to constrain the exhumation history below the unconformity. Dates from multichronometers and thermal history inversions show that the most substantial cooling of continental basement took place from ~2,100 to 1,600 Ma. Comparison with thermal history data from Laurentia, Baltica, and Amazonia suggests that protracted plate tectonics broadly modulated by supercontinent cycles, and not "snowball Earth" glaciation, is responsible for crustal exhumation below the unconformity. The most pronounced erosion evident in both the thermochronologic record and geochemical indicators of continental weathering is shown to correspond with development of Earth's first true supercontinent (Columbia), rather than with either the Cambrian explosion or the emergence of modern plate tectonics.

Great Unconformity | basement exhumation | multiple thermochronology | supercontinent cycle | Cambrian explosion

The development of the Great Unconformity (GUn) is a worldwide geological feature across which Cambrian and younger strata of almost every paleocontinent are observed to rest unconformably on Precambrian crystalline basement rocks. Because this surface records widespread erosion (1, 2) and corresponds with the emergence of complex animal life (3, 4), weathering and erosion associated with the development of the unconformity have been ascribed to the assembly and breakup of supercontinents (1, 5–7) and "snowball Earth" glaciations (2, 8, 9), and inferred to be critical in triggering modern plate tectonics (10), and the Cambrian explosion (4, 11).

In considering the origin of the GUn, the Grand Canyon (southwestern United States), where the surface was first defined by Dutton (12) more than 140 y ago, is commonly cited as the iconic example with evidence of significant crustal exhumation (1, 2, 6, 9). Considerable progress has been made in documenting the timing, magnitude, spatial extent, and driving mechanisms of denudation associated with development of the unconformity in that area, but it has been vigorously debated whether tectonic unroofing (e.g., refs. 6, 13–16) or "snowball Earth" glacial erosion (e.g., refs. 2, 8, 9) were primarily responsible. In the absence of structural complexities, it can be observed that the timing of exhumation varies even within a small area such as the Grand Canyon (e.g., refs. 14–16). The preservation of middle-late Mesoproterozoic [ca. 1,255 to 1,100 Ma Unkar Group, (17)] and late Tonian strata [ca. 775 to 729 Ma Chuar Group, (18, 19)] of the Grand Canyon Supergroup in the eastern Grand Canyon not only indicates limited basement exhumation during the early Neoproterozoic Era (15), but also speaks volumes about the weakness of "snowball Earth" as an agency of erosion in this region. In fact, limited "snowball Earth" erosion can also be observed in many other regions. In Namibia, for example, only a few tens of meters of averaged erosion can be documented beneath the late Cryogenian (Marinoan) glacial surface across a large area of the southwest Congo cratonic margin (20). Additional support for low rates of glacial erosion during "snowball Earth" conditions is provided by a global compilation of accumulation data determined from measured sections of subglacial–periglacial deposits (21). Given that development of the GUn is not confined to Laurentia alone, studies on other paleocontinents provide a way to test these expectations, and potentially, to yield new insights.

In this contribution, we present zircon and monazite U–Pb, biotite and muscovite Rb–Sr, and zircon (U–Th)/He (ZHe) thermochronologic data from basement samples from beneath

Significance

The Great Unconformity (GUn) is arguably the most iconic but enigmatic gap in Earth's stratigraphic record. Among puzzling features requiring explanation is evidence for many kilometers of exhumation and a hiatus of hundreds of millions to billions of years in continental interiors. Existing models call for either a glacial or a plate tectonic origin in the Neoproterozoic. We provide evidence that erosion below the unconformity was protracted in North China, and that the most pronounced erosion at a global scale occurred during the late Paleoproterozoic and was driven by tectonics associated with supercontinent cycle of Columbia.

Author affiliations: [a]State Key Laboratory of Continental Evolution and Early Life, and Department of Geology, Northwest University, Xi'an, Shaanxi 710069, China; [b]Department of Geosciences, University of Padova, Padova 35151, Italy; [c]Department of Earth and Environmental Sciences, and Lamont-Doherty Earth Observatory of Columbia University, Palisades, NY 10964-8000; [d]Institute of Geology and Geophysics, Chinese Academy of Sciences, Beijing 100029, China; and [e]Shaanxi Key Laboratory of Early Life and Environment, Northwest University, Xi'an, Shaanxi 710069, China

Author contributions: L.D. designed research; R.-R.Z., L.D., R.-H.W., L.G., and K.-Y.C. performed research; R.-R.Z., L.D., M.Z., N.C.-B., B.W., Z.Y., J.W., V.O., and X.Z. analyzed data; and R.-R.Z. and L.D. wrote the paper.

The authors declare no competing interest.

This article is a PNAS Direct Submission.

[1]To whom correspondence may be addressed. Email: duanl@nwu.edu.cn.

This article contains supporting information online at https://www.pnas.org/lookup/suppl/doi:10.1073/pnas.2523891123/-/DCSupplemental.

the GUn at three locations from cratonic interior and two locations near the cratonic margin of North China (Fig. 1 and *SI Appendix*, Figs. S1–S5). When supplemented by metamorphic data and stratigraphic constraints, nearly continuous thermal histories from a mid- to upper crustal level to near-surface can be constrained using a multimethod approach incorporating low-, medium-, and high-temperature thermochronology. Combined with sample-specific geologic and multiple thermochronology constraints, inverse modeling of ZHe data is used to identify spatial and temporal variations in basement cooling associated with crustal exhumation. Although ZHe data vary between samples, a comparable pulse of the most significant cooling at each sample site over hundreds of millions of years is captured by our field-based multichronometric approach. A comparison of the basement thermal and exhumation histories of interior Laurentia, Baltica, Amazonia, and North China, and analysis of globally normalized geochemical proxies of continental weathering and crustal recycling allows us to evaluate the origin of the GUn at a global scale and to explore implications of the most pronounced erosion observed below the surface.

Field Relationships

As in the case of the GUn in the western Grand Canyon region where an unconformable surface separates Archean-Mesoproterozoic basement of the Laurentian craton from overlying Cambrian strata (e.g., refs. 1, 2, 4, 22, 23), the GUn in the cratonic interior of North China represents a hiatus of more than a billion years of missing time where early Cambrian strata overlie Archean-Paleoproterozoic basement rocks (Figs. 1 and 2*A*). Consistent with the generally accepted view that the hiatus represented by unconformities is greatest in continental interiors and decreases toward continental margins, the GUn at cratonic margins in North China varies to a disconformity between late Ediacaran and early Cambrian strata with a hiatus of ~30 Myr (24, 25). Late Paleoproterozoic (Statherian) sedimentary successions overlying the basement near the cratonic margins (26) provide evidence that the basement rocks at these localities were fully exhumed prior to the Statherian (Fig. 2*B*).

Thermochronologic Record and Exhumation Histories

Zircon U–Pb dates from five basement samples range between 2,182 ± 16 Ma at Xiweikou in the south-central part of the North China craton and 1,864 ± 13 Ma at Luotuoshan in the north (Fig. 1 and *SI Appendix*, Fig. S7 and Table S1). Monazite crystals were separated only from samples Qingshuihe and Subaigou in the north and west, respectively (Fig. 1). The weighted mean ^{207}Pb/^{206}Pb ages 1,920 ± 13 Ma (MSWD = 2.6) and 1,915 ± 9 Ma (MSWD = 1.2) are indistinguishable within error (*SI Appendix*, Fig. S8 and Table S2). The Rb–Sr ages of three samples from cratonic interior are also similar (ca. 1,846 to 1,803 Ma), whereas the samples near the margin are either a little older (1,920 ± 36 Ma) or much younger (1,656 Ma ± 18 Ma) than those from interior (*SI Appendix*, Fig. S9 and Table S3).

ZHe results from 23 grains from 5 samples show generally high dispersion and range from 1,357 ± 27 Ma to 23.89 ± 0.30 Ma over an eU span of 49 to 1,008 ppm (*SI Appendix*, Table S4). These data fall on a generally coherent and negative date-eU trend, with the oldest ZHe dates corresponding to low-eU grains (Fig. 3*A*), suggesting a shared thermal history. None of the samples show an obvious correlation between ZHe date and equivalent spherical radius (Fig. 3*B*), suggesting that the observed ZHe date does not directly relate to grain size.

In agreement with documented dates of multichronometers themselves (Fig. 4*A*), thermal history simulations constrained by sample-specific geologic and multiple thermochronologic data (*SI Appendix*, Table S5) point to an earlier rapid cooling episode ranging from ~2,100 Ma to ~1,600 Ma, followed by a slower phase of cooling within the cratonic interior, and monotonic cooling and/or burial reheating at the cratonic margin during Meso- to Neoproterozoic time (Fig. 4 *B*–*F*). Although synchronous exhumation across part of North China during the Cryogenian is permitted by regions of t–T space for samples within cratonic interiors (Fig. 4 *B*–*D*), no enhanced cooling is shown by highly resolved paths with relatively high-probability from any single sample (Fig. 4 *B*–*F*).

Protracted Erosion Below the GUn

Previous work has led to the idea that major erosion below the GUn was most likely a single pronounced, worldwide exhumation event (2, 4, 10). However, this idea has already been questioned by a growing number of thermochronology studies focused on the exhumation of ancient crystalline basement and development of the GUn erosion surface in Laurentia (e.g., refs. 13–16). A combination of geologic context, multiple thermochronometers, and inverse ZHe modeling indicates synchronized multistage exhumation of North China basement from an average crustal depth of ~25 km (865 to 750 °C at 9.8 to 5.6 kbar; *SI Appendix*, Fig. S10) to the surface. Although no Paleoproterozoic ZHe date was obtained, ZHe modeling combined with additional chronometers from Paleoproterozoic basement

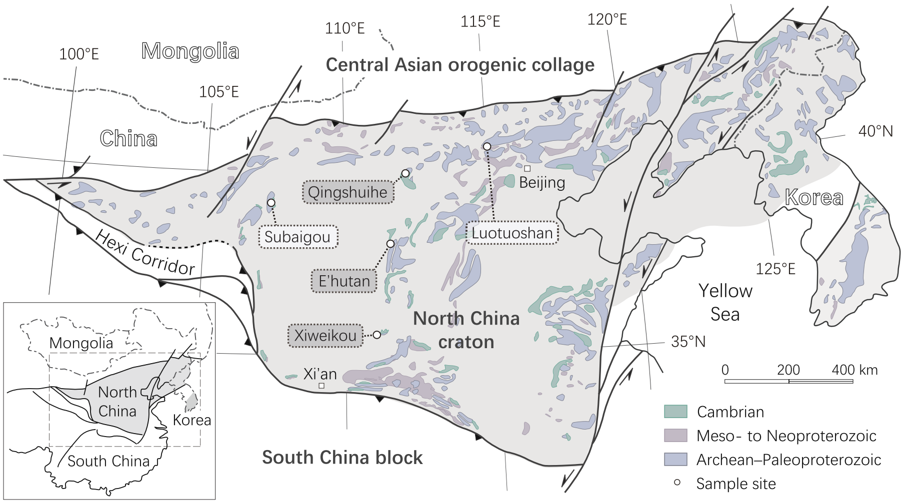

Fig. 1. Tectonic framework of North China showing the distribution of Archean to Paleoproterozoic basement, Meso- to Neoproterozoic and Cambrian strata with the sites of sampled sections. The Qingshuihe, E'hutan, and Xiweikou sections lie in the cratonic interior. Samples Subaigou and Luotuoshan represent the cratonic margin. Geologic and petrologic details for each sample are provided in *SI Appendix*, Figs. S1–S6.

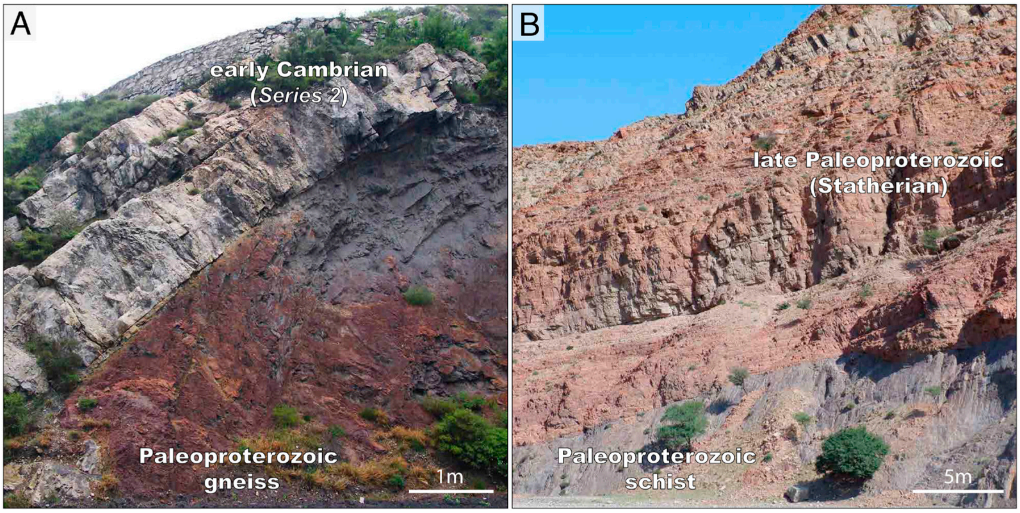

Fig. 2. Field relationships of the Great Unconformity (GUn) in North China. (*A*) The GUn across cratonic interior at the Xiweikou section (GPS: 35°43′42.33″N, 110°43′11.85″E) in the southernmost Lüliang Mountains, with ~520-Myr-old nearshore sandstone overlying 2,182-Myr-old granitic basement. (*B*) The basement nonconformity near cratonic margin at the Subaigou section (GPS: 39°10′13.65″N, 106°57′49.14″E) in the western part of Inner Mongolia (northwest China), with ~1,750 to ~1,600-Myr-old nearshore sandstone on 2,014-Myr-old basement rocks of schist.

provides strong evidence that most erosion below the GUn across large swaths of North China occurred prior to the onset of Neoproterozoic "snowball Earth" conditions, and overlaps with the timing of the Columbia supercontinent cycle (27, 30). The major cooling trend from ~2,100 Ma to ~1,600 Ma revealed by dates of higher temperature isotopic systems indicates at least ~370 °C of cooling during this period, and requires a ~12.3 km average exhumation within cratonic interior of the North China assuming a geothermal gradient of 30 °C/km. The major pulse of Paleoproterozoic cooling and unroofing shown by our samples may be associated with regional tectonic events representing Columbia amalgamation and break-up that are evident around much of the North China, with the amalgamation of the eastern and western blocks during Paleoproterozoic Trans-North China collision (31), Andean-style convergent-margin tectonism and subsequent ca. 1.9 to 1.85 Ga collision along the craton's northern edge in Inner Mongolia–Northern Hebei (32, 33). Thermochronological evidence for the timing of exhumation is consistent with the presence of late Paleoproterozoic and early Mesoproterozoic strata unconformably overlying basement across the northern and southern margins (34, 35), implying that the interior of North China may have undergone weathering and erosion during this phase of the supercontinent cycle.

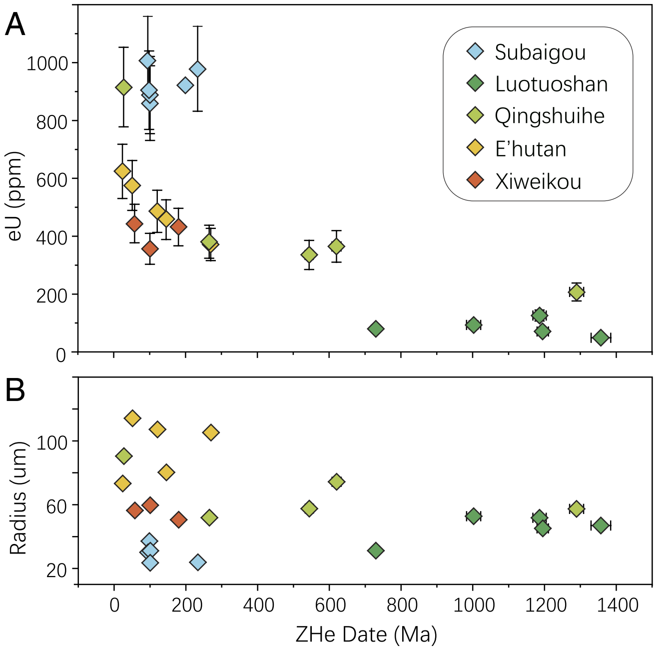

Fig. 3. Zircon (U-Th)/He (ZHe) data. (*A*) ZHe date versus effective uranium concentration (eU) plot for all samples. Uncertainties of eU are conservatively assumed to be 15%. Uncertainties on individual ZHe dates are reported at 2σ, and most are smaller than the datum marker size. (*B*) Plot of ZHe date versus spherical grain radius.

It is now clear that reburied basement near the cratonic margin did not undergo significant cooling during Meso- to Neoproterozoic eras. In addition, all samples from within the cratonic interior display a prolonged and slower phase of cooling. Rb-Sr data and the geologic context indicate a maximum of ~380 °C and a minimum of ~280 °C cooling from ~1,600 Ma to ~520 Ma, requiring no more than ~12.7 km (at least ~9.3 km) of averaged basement exhumation. Although ZHe modeling shows that there was no enhanced cooling during any part of this phase, the preservation of middle Mesoproterozoic to Tonian (ca. 1,357 Ma to ca. 730 Ma) and Ediacaran (ca. 620 Ma to ca. 544 Ma), but not including any Cryogenian, low-temperature ZHe dates is significant. These mid-Mesoproterozoic to Tonian ZHe dates generally match the timing of the Rodinia supercontinent cycle. The placement of the North China against Laurentia has been proposed on the basis of Mesoproterozoic and Tonian paleomagnetic constraints (e.g., refs. 36–38) and provenance analyses of Mesoproterozoic–Neoproterozoic basins in southeast North China (e.g, refs. 39, 40). For these reasons, therefore, we tentatively propose mechanisms associated with Rodinia supercontinent assembly or breakup processes as the cause of limited exhumation, although Grenville-age orogenic records are poorly represented in present-day North China (41). Additional support for this interpretation, and a link between North China and the breakup of Rodinia (42), is provided by a proposed connection between the ca. 775 Ma dikes in North China and the ca. 778 Ma Gunbarrel large igneous province in Laurentia (36).

Two Ediacaran ZHe dates (ca. 620 Ma and ca. 544 Ma) obtained from one sample from the northern part of the cratonic interior are consistent with published ZHe evidence for rapid cooling between ca. 630 to 570 Ma obtained from a borehole sample of Paleoproterozoic sandstone from the northwestern interior of North China (43). Cooling through ~180 °C at ca. 544 ± 11 Ma is broadly

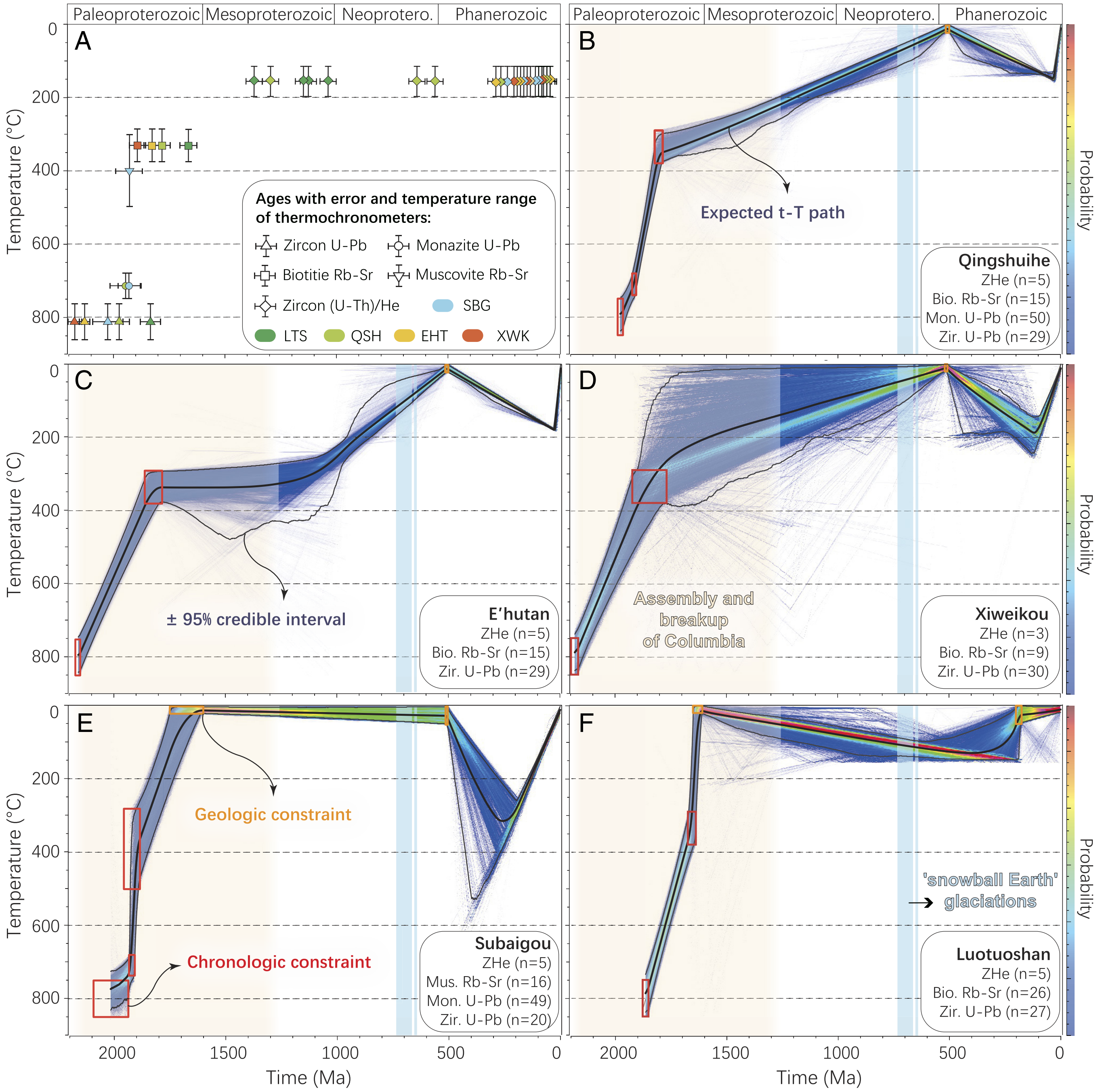

Fig. 4. Thermochronologic and thermal history model results. (*A*) Zircon and monazite U–Pb, biotite/muscovite Rb–Sr, and zircon (U–Th)/He (ZHe) age data obtained from five basement samples. (*B*–*F*) QTQt time-temperature (t–T) inversions of new thermochronologic data showing consistent thermal histories with rapid late Paleoproterozoic cooling. Colors refer to the probability of a thermal history to pass through a given point. Thin and thick black lines show the 95% credible intervals of the expected model and a weighted average of all accepted models (weighted by the posterior probability of each model). All models enforced geologic (orange boxes) and chronologic constraints (red boxes). Episodes of Columbia supercontinent cycle (27) and "snowball Earth" glaciations (28, 29) are highlighted with pale orange and airy blue vertical bands, respectively.

coincident the timing of late Ediacaran (ca. 550 Ma) glaciation that is evident in North China (24), with widespread glaciogenic deposits intermittently exposed over 2,000 km across the southern margin (44). Thermochronologic data, therefore, permit a glacial contribution to Ediacaran exhumation during development of the GUn, but snowball conditions do not appear to have played a critical role.

Erosion Beneath the GUn At a Global Scale

New data from the North China interior show that the thermal history of basement rocks beneath the GUn is characterized by a broad spatial pattern and synchroneity of the most significant cooling. This is apparently different from key results from thermochronologic studies of the Precambrian thermal history of Laurentian basement, where exhumation rates and timing appear to have varied regionally (e.g., refs. 5–9, 13, 16, 45, 46). Therefore, obtaining a full picture of the origin of the GUn requires a holistic consideration from a global perspective.

Depending on medium- to low-temperature thermochronologic records from the basement of Laurentia (5–9, 13–16, 45–47) and asserted relations to geochemical indicators of crustal recycling in zircons (2), numerous models have been proposed to account for many kilometers of continental erosion below the GUn. Existing nonmutually exclusive models can be divided into two schools of thought with respect to mechanisms: 1) rapid Cryogenian erosion during "snowball Earth" glaciations (e.g., refs. 2, 9, 10); and 2) long-term exhumation induced by tectonics and geodynamics associated with Rodinia supercontinent assembly and breakup (e.g., refs. 5–7, 13, 16, 45, 47). New data from North China indicate that development of the GUn was due to tectonically and geodynamically controlled exhumation, broadly modulated by supercontinent cycles (5–7, 13–16, 45–47). However, most exhumation below the GUn in interior North China occurred before the onset of the Rodinia supercontinent cycle, with basement denudation between ~1.2 Ga and deposition of the basal Cambrian sandstone at ~520 Ma eclipsed in magnitude by a single pulse erosion during the late Paleoproterozoic.

Most recent thermochronologic studies carried out in the Laurentian craton have been aimed at discriminating among different hypotheses for sub-GUn exhumation by means of medium and low-temperature thermochronology. ZHe data patterns, as well as K-feldspar multiple diffusion domain ^{40}Ar-^{39}Ar and apatite fission-track (AFT) data from different areas of the Laurentia are sufficient to constrain upper-crustal to near-surface temperature-time (<350 °C) histories of basement (e.g., refs. 5–9, 13, 16, 45, 47), and to test the hypothesis that global Neoproterozoic glacial erosion removed 3 to 5 km of material during 717 to 635 Ma "snowball Earth" events (2). However, the pressure recorded by basement rocks in the Grand Canyon and interior North China was regionally more than 8 kbar (48, 49), which is equivalent to a mid-crustal level depth of ~25 km. Therefore, any unifying theory for the origin of the GUn must contend with reported dates of higher temperature systems extending to mid-crustal level, and evaluate the pattern of basement exhumation in different paleocontinents (8).

Fig. 5*A* summarizes the mid-crustal to near-surface thermal histories of Precambrian basement in North China, Baltica, Amazonia, and Laurentia in the form of expected t–T paths. In each of these study regions where the Sauk sequence (the first continental-scale marine transgression of the Phanerozoic, 22, 50) directly overlies basement, key results from thermochronologic studies show a protracted, multistoried history of basement exhumation that appears to have varied from region to region (Fig. 5*A*). The model relating exhumation to Rodinia aggregation may be valid for the southern and central Canadian Shield (e.g., Superior Province and Grenville Province), and the southern Rocky Mountains (e.g., Pikes Peak batholith) owing to its proximity to the Neoproterozoic Grenville orogen. New constraints from North China compare well with existing thermochronologic record and Precambrian history of Baltica (51–53), Amazonia (54–57), and the western Grand Canyon (17, 58, 59), Ozark Plateau (5, 60, 61) and Laramide ranges (62, 63) of Laurentia in mid- to upper-crustal level, and the emerging full picture is one of common enhanced exhumation spanned the late Paleoproterozoic (Fig. 5*A*). More than half of the protracted Precambrian exhumation (~13 km as a result of over ~400 °C of cooling) occurred during this interval. Insofar as the Columbia supercontinent is distinguished by global-scale evidence for subduction and the onset of a fully linked global plate tectonic network (27, 64), we prefer a model in which globally increased exhumation related broadly to supercontinent assembly is responsible for most of the GUn denudation within interiors of core crustal blocks of the nearly entire continent. Support for this interpretation is provided by the preservation of large outliers of flat-lying Statherian sandstone on many cratons around the world, including the Roraima Supergroup of the Guiana Shield (65), the Katherine River Group of northern Australia (66), the Athabasca Group and Thelon Formation of northern Laurentia (67). These clearly demonstrate that Archean-Paleoproterozoic basement rocks were exhumed to the surface soon after the aggregation of the Columbia supercontinent. Multiple phases of erosion during the Rodinia supercontinent cycle (5–7, 13–16, 45–47), "snowball Earth" glaciations (2, 9, 10), and Sauk transgression (4) undoubtedly contributed to development of the GUn, but none of them provides the principal explanation across multiple continents.

Implications for Earth-Life System

As Charles Darwin was aware in the mid-19th century, the seemingly rapid diversification of life in the Cambrian is greatly accentuated by the presence of an unconformity at many locations. The GUn hiatus, referred to as Walcott's "Lipalian" interval, was thought to represent the span during which the Cambrian fauna developed, but without leaving much of a geological record (3). However, studies of more complete sections on many continents had already led to a very different view: that the emergence and diversification of animals did in fact occur over a relatively short interval of time (several tens of millions of years, 77). The interval has received recent attention because continental erosion is hypothesized to have provided critical elements and nutrients to the oceans, and a mechanism for sparking the Cambrian Explosion (4). Based on a new modeling approach to geochemical signals of crustal recycling, Keller et al. (2) presented an intriguing hypothesis that erosion below the GUn was driven mostly by "snowball Earth" glaciations. Subsequently, the lubricating effect of unconsolidated sediments in subduction channels (78) led Sobolev and Brown (10) to suggest that an increased flux of sediments available for the stabilization of subduction following unprecedented surface erosion associated with the "snowball Earth" glaciation kick-started the modern expression of plate tectonics.

Geochemical support for these hypotheses is said to include seawater strontium (Sr) isotope (^{87}Sr/^{86}Sr) evidence for enhanced continental erosion (Fig. 5*B*), crustal recycling signals provided by Hf and O isotopes in zircon, and neodymium (Nd) in whole-rock sediments and granitoids (Fig. 5*C*). The correlation between a nadir in globally averaged zircon εHf and a positive δ^{18}O anomaly (Fig. 5*C*) was considered to represent a paleoerosion proxy preserved in Earth's igneous record (2). Old crustal material from the Earth's surface delivered by "snowball Earth" glaciation to oceanic trenches and subducted would have led to an unprecedented increase in the recycling of continental crust in new magmas (2). Furthermore, the time interval of Neoproterozoic "snowball Earth" glaciations (about 717 to 635 Myr ago, 28, 29), marked by a consistent increase in Sr and δ^{18}O in zircon and by a decrease in Hf and Nd, was interpreted to correspond to the timing of enhanced surface erosion and subduction lubrication events (10). However, interpretation of extreme erosion during "snowball Earth" events obtained from modeling a global compilation of zircon εHf and δ^{18}O data (2, 10) has been questioned due to geographically biased sample distributions and omission of the tectonic context of the data (75, 79). Resampling inversely to data density in an attempt to augment low density gaps in the global record (e.g., ref. 2) in turn obfuscates tectonic signals and artificially weights outliers (79). Specifically, the positive anomalies of zircon δ^{18}O and highly enriched εHf once attributed to "snowball Earth" erosion (2) have recently been reinterpreted to record upper-plate, supracrustal sources of Gondwana (75, 79), and become less pronounced in a recent global compilation after removal of isolated data contributions (Fig. 5*C*).

As pointed out by Macdonald et al. (47), there is a ~85 Myr temporal lag between the "snowball Earth" glaciation and peaks of the largest global Hf and O isotope excursions (Fig. 5*C*). Instead, the timing of the all-time maximum in zircon δ^{18}O and seawater ^{87}Sr/^{86}Sr values, as well as the nadir in zircon εHf, is

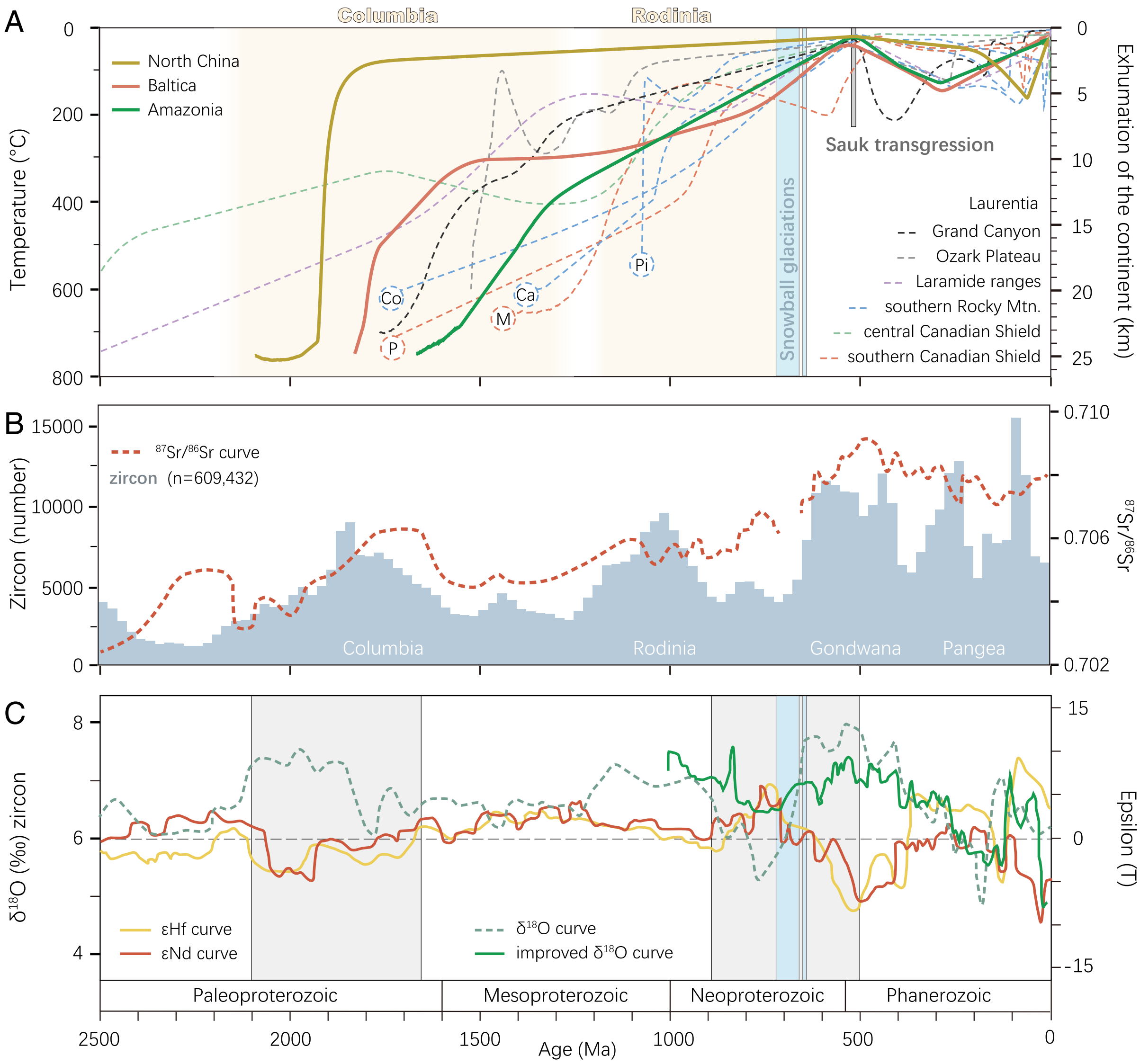

Fig. 5. Summary of inverse thermal histories of cratonic interiors in the context of Earth systems evolution. (*A*) Synoptic thermal histories of interior North China, Baltica, Amazonia, and Laurentia show significant cooling during supercontinent cycles of Columbia and Rodinia (pale orange bands) prior to snowball glaciation (airy blue bands). Timeline of supercontinent Columbia and Rodinia highlighted with pale orange vertical bands is from ref. 27. Thermal histories are shown by expected t–T paths, which represent "preferred" single path within 95% credible intervals of the expected model (68). T–t paths of Baltica and Amazonia are from Paleoproterozoic basement in the Laxemar region of the Fennoscandian Shield (Sweden, 51) and late Paleoproterozoic to early Mesoproterozoic Rio Negro–Juruena basement of the western Guiana Shield (Colombia, 69). T–t paths of Laurentia are from Paleoproterozoic Granite Gorge Metamorphic suite and granitoids of the western Grand Canyon (Arizona, 14, 15), Mesoproterozoic granitic batholith of the St. Francois Mountains of the Ozark Plateau (Missouri, 5), Archean basement of the Laramide ranges (Wyoming, 70), Paleoproterozoic crystalline rocks of the Cookes Range (New Mexico, 71), Mesoproterozoic basement of the Carrizo Mountains (Texas, 71), and late Mesoproterozoic Pike Peak batholith (Colorado, 6) of the southern Rocky Mountains, Neoarchean basement of the central Canadian Shield (Manitoba, Canada, 9), Paleoproterozoic Superior Province and Mesoproterozoic Grenville Province of the southern Canadian Shield (Ontario, Canada, 46). Thermal histories of these regions are depicted to represent Laurentia because thermochronologic data are available for basement rocks directly overlain by Sauk sequence strata. Ca, Carrizo Mountains; Co, Cookes Range; M, Mesoproterozoic Grenville Province; P, Paleoproterozoic Superior Province; Pi, Pikes Peak batholith. QTQt time–temperature inversions of published thermochronologic data showing expected thermal history paths of these regions are in *SI Appendix*, Figs. S11–S22. (*B*) The seawater strontium isotope ratios (^{87}Sr/^{86}Sr) curve (72) and histograms of global detrital zircon age distributions (73) showing several populations in their U-Pb crystallization ages over the course of Earth history that are very similar to supercontinent cycles. Bin width is 25 Myr. (*C*) The cadet blue dashed curve shows the global running median of zircon δ^{18}O data from recent sediment (74). The green solid curve shows a recently improved curve of zircon δ^{18}O from 1,000 Ma to present after removal of isolated data contributions (75). Yellow and brown lines represent the global running median of εHf for detrital zircons and εNd for whole-rock sediments and granitoids (76), respectively. Gray rectangles show periods of major rises of ^{87}Sr/^{86}Sr ratios through Earth history.

more closely aligned with the Cambrian Sauk transgression (Fig. 5; 22, 50). It has also been noted that the long-term increase of seawater ^{87}Sr/^{86}Sr values is not only restricted to the Neoproterozoic Era, but observed during times of assembly of the supercontinent Colombia and Rodinia (72, 80, Fig. 5*B*). Associated with supercontinent amalgamation, tectonic-related uplift would have facilitated erosion and chemical weathering, and therefore, increased the input of radiogenic Sr flux to the ocean. Further complications arise from the fact that seawater ^{87}Sr/^{86}Sr reflects not only changes in the relative contributions of more radiogenic riverine input from continental weathering and less radiogenic hydrothermal activity but also the isotopic composition of rocks undergoing weathering (72). The increase in seawater ^{87}Sr/^{86}Sr values during the supercontinent cycle of Columbia (Fig. 5*B*) is distinguished by a long-term increase in εHf and εNd values, and a decrease in δ^{18}O values with time

(Fig. 5C), reflecting more significant input of juvenile crust with unradiogenic Sr isotope ratios (72). On the basis of these data, a sharp rise of seawater $^{87}Sr/^{86}Sr$ ratios during the late Paleoproterozoic is thought to be driven primarily by a sustained increase in continental weathering rate. In contrast, an increase of seawater $^{87}Sr/^{86}Sr$ during the Neoproterozoic was associated with a decrease in εHf and εNd values and an increase in $\delta^{18}O$ values, indicating more contribution of radiogenic riverine input from continental weathering. Therefore, a long-term rise of seawater $^{87}Sr/^{86}Sr$ during the Neoproterozoic, especially abrupt increases in the aftermath of early Cryogenian (Sturtian) and late Cryogenian (Marinoan) glaciations, should be treated cautiously.

Taken together, significant basement exhumation concurrent with supercontinent assembly of Columbia during the late Paleoproterozoic is evident in both the global thermochronologic record and geochemical indicators of continental weathering and crustal recycling. Our findings provide evidence that protracted plate tectonics broadly modulated by supercontinent cycles, and not "snowball Earth" glaciations, represents the main driver of crustal exhumation below the GUn (5–7, 13–16, 45–47). Unlike previously documented thermochronologic constraints on the origin of the GUn in the southern Rocky Mountains and Canadian Shield of Laurentia, evidence from multiple thermochronometers synthesized here strongly suggests that mechanisms driving most of the GUn denudation date from the late Paleoproterozoic, much earlier than the Cambrian Explosion of life or the onset of modern plate tectonics (4, 10).

Materials and Methods

Sample Selection and Preparation. In an effort to capture the cooling history of basement rocks throughout much of the North China craton, samples were collected from five outcrop sections (Fig. 1). These sections were chosen on the basis of quality of exposure of the basement nonconformity, and they are arranged equally spaced across a vast region of both the interior and margin of the craton. At three sections (Qingshuihe, E'hutan, and Xiweikou) in the cartonic interior, samples were collected ~2 to 10 m below the GUn (Fig. 2A). At two sections (Subaigou and Luotuoshan) close to the cratonic margin, samples were collected ~5 m below the basement nonconformity (Fig. 2B) where the basement is overlain by ~1,750 to 1,600-Myr-old Changchengnian (Statherian) rocks. Details of the geology in each section are provided in *SI Appendix*, Figs. S1-S5. Among these sections, basement rocks in Subaigou are quartz mica schist composed of quartz (60%), mica (40%), with accessory ilmenite, zircon, and monazite (*SI Appendix*, Fig. S6). Biotite-plagioclase gneiss at the other four sections is mineralogically similar: biotite (10 to 15%), plagioclase (50 to 60%), quartz (25 to 50%), with accessory apatite, ilmenite, zircon, and sphene (*SI Appendix*, Fig. S6).

A collection of basement rocks from five outcrops was analyzed for zircon and monazite U-Pb, biotite and muscovite Rb–Sr, and zircon (U-Th)/He (ZHe) thermochronology. Zircon and monazite crystals were extracted by standard density and magnetic separation techniques and then purified by hand picking under a binocular microscope. Representative zircon and monazite grains were mounted in epoxy resin discs, then polished to expose crystal centers. All analyzed zircon and monazite grains were documented using cathodoluminescence imaging and backscattered electron scanning microscopy analysis for internal morphology in order to identify internal textures and to guide spot selection for U-Pb isotopic analyses, using a Mono CL3+ attached to a scanning electron microscope (Quanta 400 FEG) and a JXA-8230 electron microprobe equipped with five wavelength-dispersive spectrometers at State Key Laboratory of Continental Evolution and Early Life (SKLCEEL) at Northwest University, Xi'an, China.

Zircon U–Pb. Using CL images, approximately 20 to 30 selected zircon grains were analyzed from each sample using laser ablation–inductively coupled plasma–mass spectrometry (LA-ICP-MS) at SKLCEEL, Northwest University. The ICP-MS used is a Varian 820-MS, and the analyses involve ablation of zircon with the GeoLas 2005 laser ablation system operating at a wavelength of 193 nm, following the analytical procedures summarized in ref. 81. The laser beam was focused to a diameter of 44 μm, with the frequency of 10 Hz. Raw count rates were measured for ^{29}Si, ^{204}Pb, ^{206}Pb, ^{207}Pb, ^{208}Pb, ^{232}Th and ^{238}U. U, Th, and Pb concentrations were calibrated by using ^{29}Si as an internal standard and NIST 610 as the reference standard. $^{207}Pb/^{206}Pb$, $^{206}Pb/^{238}U$, $^{207}Pb/^{235}U$, and $^{208}Pb/^{232}Th$ ratios were corrected for both instrumental mass bias and depth-dependent elemental and isotopic fractionation using Harvard zircon 91500 as external standard. Age calculations and plotting of concordia diagrams were made using IsoplotR (82) for results with 1σ errors (*SI Appendix*, Fig. S7 and Table S1).

Monazite U–Pb. U–Pb dating of monazite was done using an Agilent 7900 ICP-MS coupled with a COMPexPro 102 ArF excimer laser and a MicroLas optical system at the Wuhan SampleSolution Analytical Technology Co., Ltd., Wuhan, China. Fifty spot analyses were done in samples Qingshuihe and Subaigou. Helium was applied as a carrier gas, and argon was used as the make-up gas and mixed with the carrier gas via a T-connector before entering the ICP. The laser beam was focused to a diameter of 16 μm, with the frequency of 2 Hz. A "wire" signal smoothing device is included in the laser ablation system, by which smooth signals are produced even at very low laser repetition rates down to 1 Hz (83). Monazite standard material 44069 and NIST610 glass were used as external standards for U-Pb dating and trace element calibration, respectively. Each analysis incorporated a background acquisition of approximately 20 to 30 s followed by 45 s of data acquisition from the sample. The excel-based software ICPMSDataCal was used to perform data processing for trace element concentrations and U–Pb ages with 1σ errors (84, *SI Appendix*, Fig. S8 and Table S2).

Mica Rb–Sr. In situ mica Rb–Sr isotopic compositions were collected from polished thin section using an Agilent 8900 triple quadrupole mass spectrometer coupled with a femtosecond laser ablation system (NWR FemtoUC) at SKLCEEL, Northwest University. According to the mineral assemblage of dated samples, muscovite was analyzed from sample Xiweikou, while biotite was analyzed from the other four samples. The mass spectrometer was operated in collision/reaction cell (CRC) mode using NO_2 as the reaction gas in the collision cell to enable measurement of Rb and Sr isotopes (85, 86). $^{87}Sr/^{86}Sr$ and $^{87}Rb/^{86}Sr$ ratios were drift-corrected and calibrated against SRM 610-2 and BHVO-2G-3. Data acquisition employed time-resolved analysis (TRA) mode with an individual point integration time of 0.075 s and total acquisition duration of 90 s (including 25 s gas blank and 60 s sample ablation). The analytical conditions were established according to the approach outlined in refs. 87, 88. The date is calculated by the traditional approach of laser-based Rb-Sr isochron dating using Iolite 4 (89), in which individual laser spots are fully integrated and plotted on an isochron diagram. All ages and uncertainties are presented with 2SE (SE) level of confidence (*SI Appendix*, Fig. S9 and Table S3).

Zircon (U-Th)/He. The Zircon (U-Th)/He analyses were performed at the University of Arizona Radiogenic Helium Dating Laboratory following the procedures of Reiners et al. (90). Prospective zircon grains were selected using a Leica M165 binocular microscope to be as large and euhedral as possible, and free of visible inclusions or fractures. The Zircon (U-Th)/He dataset is composed of twenty-three single zircon grain aliquots, including 3 for sample Xiweikou, and 5 for each of the other four samples. Selected crystals were packed individually and loaded into Nb tubes for U-Th-He analyses and heated for a preliminary gas extraction using a CO_2 laser to ~1,250 °C for 15 min. The grains were then subjected to two additional extractions at higher temperatures for 20 min to purge any residual ^4He gas. The released ^4He gas was spiked with a known volume of ^3He and measured with a quadrupole mass spectrometer. Zircon grains were then dissolved in an acid solution (91) and the U, Th, and Zr isotopes were measured with an Element 2 high-resolution ICP-MS. Alpha ejection corrections based on volume dimensions for individual grains were applied for a corrected Zircon (U-Th)/He date (92). All Zircon (U-Th)/He dates are presented in *SI Appendix*, Table S4.

Inverse Thermal History Modeling. To resolve the thermal history of the basement rocks, we performed inverse thermal modeling of ZHe data using the program QTQt by Gallagher (68). The modeling incorporates a Bayesian transdimensional Markov Chain Monte Carlo inversion technique to generate an "expected model" of the sample history based on a weighted average of the posterior probability distribution by iterating $\geq 10^6$ thermal histories within a set of model space based on the measured data (68). This posterior distribution can also be used to define the 95% credible intervals that provide a measure of uncertainty. The aim of the transdimensional sampling is to try to balance model complexity with fitting the data, that is to avoid overfitting the data with overly complex models. The Bayesian approach deals with this implicitly. Full details on the methodology of these approaches, and description of the mathematical and statistical underpinnings of the program are provided by refs. 68, 93.

Input data included single-grain data and "prior" time-temperature box. (U-Th)/He dates, F_T-equivalent spherical radius, and U, Th, Sm, and He concentrations for each sample were input individually with 2 s analytical uncertainty applied as the date uncertainty and no resampling of date or uncertainty. The radiation damage and annealing models applied were the zircon radiation damage accumulation and annealing model (ZRDAAM) of Guenthner et al. (94). The "prior" box required by QTQt was set to span the age of the sample and temperature range dictated by the constraint boxes. The "prior" box thus differed for each sample and corresponds to a time range from the oldest thermochronometer age to present and a temperature range from crystallization temperature to 0 °C. Given the importance of independent geologic constraints for interpreting and modeling thermochronology data (95–97), models (individual t–T "paths") are constructed from geologic observations and the other thermochronology data in the form of geologic and chronologic constraint boxes (Fig. 4). Geologic constraints consist of temperatures corresponding to the exhumation of basement sample to the surface (0 to 20 °C), with the age constrained by directly overlying strata (*SI Appendix*, Table S5; ~520 Ma across cratonic interior, and ~1,750 to 1,600 Ma at margins). Chronologic data that vary for each sample were also input into the model as a constrained area by adopting a conservative age and closure temperature range (*SI Appendix*, Table S5). All data used to impose t–T constraints are available in *SI Appendix*, Table S5.

Previously published ZHe and AFT data from basement rocks below the GUn erosion surface are summarized (*SI Appendix*, Tables S6 and S7) and remodeled (*SI Appendix*, Figs. S11–S22). For QTQt simulation using AFT data, the multikinetic apatite fission track annealing model of Ketcham et al. (98), with the etch pit diameter (D_{par}) as kinetic parameter, was used. Geologic and chronologic data used to impose t–T constraints are summarized in *SI Appendix*, Table S8.

Phase Equilibrium Modeling. To better constrain the depth from which basement samples were exhumed, and to confirm that the detected cooling is not a result of perturbations of geothermal gradient that may have nothing to do with crustal exhumation (e.g., ref. 99), the pressure–temperature condition of the selected basement sample (Qingshuihe) is determined by phase equilibrium modeling on the basis of petrography, bulk and mineral geochemistry (*SI Appendix*, Tables S9 and S10). Bulk chemical compositions were determined by wavelength-dispersive X-ray fluorescence (XRF) spectrometry (Rigaku RIX 2100) on a fused bead at the SKLCEEL, Northwest University, Xi'an. Mineral compositions were analyzed using the JEOL JXA-8230 electron microprobe SKLCEEL, Northwest University. The operating conditions were 2 μm beam size, 15 kV acceleration voltage, and 10 nA beam current.

Phase equilibrium modeling was carried out in the system NCKFMASTO (Na_2O–CaO–K_2O–FeO–MgO–Al_2O_3–SiO_2–H_2O–TiO_2–O_2) using the Theriak-Domino software (100), with the dataset file ds62 (adopted from the Thermocalc database ds62 by Holland and Powell, 101, 102). The adopted activity–composition (a–x) models are listed in the following: chlorite, garnet, chloritoid, muscovite, biotite, cordierite, orthopyroxene, ilmenite, and melt (103), plagioclase and K-feldspar (104), as well as magnetite and spinel (105). Kyanite, rutile, and quartz were treated as pure mineral phases. FeO content was measured by Fe^{2+} titration, and Fe_2O_3 contents were calculated by difference. H_2O contents were adopted using T–X_{H2O} pseudosection, so that the final retrograde mineral phase was stable just above the post-melt-loss solidus (106). The normalized molar bulk-rock compositions used for the phase equilibrium modeling are given in *SI Appendix*, Table S10.

Data, Materials, and Software Availability. Inverse thermal history and phase equilibrium modeling programs used in the study can be downloaded from the following links: QTQt v.5.9.0: https://www.thermonet.cnrs.fr/en/software-programs/qtqt-software/qtqt-version-and-update/ (107), and Theriak-Domino: https://titan.minpet.unibas.ch/minpet/theriak/theruser.html (108). Thermocalc database ds62 are available at https://hpxeosandthermocalc.org/the-hpx-eos/hpx-eos-implementation/?_refluxos=a10 (109). All other data are included in the manuscript and/or *SI Appendix*.

ACKNOWLEDGMENTS. This work was supported by the National Natural Science Foundation of China (U24A20601, 91955311, and 42072258), the Center for International Cooperation and Disciplinary Innovation (the 111 Project, D17013), Key Science and Technology Project of Changqing Oilfield Company of PetroChina (2024D1JC06), and the MOST Special Fund from the State Key Laboratory of Continental Evolution and Early Life at Northwest University. Sincere thanks to Kerry Gallagher, Barra Peak, Guangwei Li, and Yaling Tao for advice on thermal history modeling. We thank the handling editor, Paul Hoffman, and an anonymous reviewer for constructive comments and insightful suggestions that improved the clarity and quality of the manuscript.

1. K. E. Karlstrom, J. M. Timmons, "Many unconformities make one 'Great Unconformity'" in *Grand Canyon Geology: Two Billion Years of Earth's History*, K. E. Karlstrom, J. M. Timmons, Eds. (Geological Society of America, 2012), vol. 489, pp. 73–79.
2. C. B. Keller *et al.*, Neoproterozoic glacial origin of the Great Unconformity. *Proc. Natl. Acad. Sci. U.S.A.* **116**, 1136–1145 (2019).
3. C. D. Walcott, Abrupt appearance of the Cambrian fauna on the North American continent. *Smithsonian Misc. Collect.* **57**, 1–16 (1910).
4. S. E. Peters, R. R. Gaines, Formation of the "Great Unconformity" as a trigger for the Cambrian explosion. *Nature* **484**, 363–366 (2012).
5. M. S. DeLucia, W. R. Guenthner, S. Marshak, S. N. Thomson, A. K. Ault, Thermochronology links denudation of the Great Unconformity surface to the supercontinent cycle and snowball earth. *Geology* **46**, 167–170 (2018).
6. R. M. Flowers, F. A. MacDonald, C. S. Siddoway, R. Havranek, Diachronous development of Great Unconformities before Neoproterozoic Snowball Earth. *Proc. Natl. Acad. Sci. U.S.A.* **117**, 10172–10180 (2020).
7. J. W. Ricketts *et al.*, Tectonic controls on basement exhumation in the southern Rocky Mountains (United States): The power of combined zircon (U-Th)/He and K-feldspar $^{40}Ar/^{39}Ar$ thermochronology. *Geology* **49**, 1187–1192 (2021).
8. K. T. McDannell, C. B. Keller, W. R. Guenthner, P. K. Zeitler, D. L. Shuster, Thermochronologic constraints on the origin of the Great Unconformity. *Proc. Natl. Acad. Sci. U.S.A.* **119**, e2118682119 (2022).
9. K. T. McDannell, C. B. Keller, Cryogenian glacial erosion of the central Canadian Shield: The "late" Great Unconformity on thin ice. *Geology* **50**, 1336–1340 (2022).
10. S. V. Sobolev, M. Brown, Surface erosion events controlled the evolution of plate tectonics on earth. *Nature* **570**, 52–57 (2019).
11. S. E. Peters, D. P. Quinn, J. M. Husson, R. R. Gaines, Macrostratigraphy: Insights into cyclic and secular evolution of the Earth-life system. *Annu. Rev. Earth Planet. Sci.* **50**, 419–449 (2022).
12. C. Dutton, Tertiary history of the Grand Canyon district. *Am. J. Sci.* **S3–24**, 81–89 (1882).
13. C. P. Sturrock, R. M. Flowers, F. A. Macdonald, The late great unconformity of the Central Canadian Shield. *Geochem. Geophys. Geosyst.* **22**, 1–22 (2021).
14. B. A. Peak, R. M. Flowers, F. A. Macdonald, J. M. Cottle, Zircon (U-Th)/He thermochronology reveals pre-Great Unconformity paleotopography in the Grand Canyon region, USA. *Geology* **49**, 1462–1466 (2021).
15. O. G. Thurston *et al.*, Deep-time thermal history of the Great Unconformity in the Grand Canyon, USA: Combined zircon (U-Th)/He and K-feldspar $^{40}Ar/^{39}Ar$ thermochronometers. *Geol. Soc. Am. Bull.* **136**, 1–21 (2024).
16. O. G. Thurston *et al.*, Zircon (U-Th)/He thermochronology of Grand Canyon resolves 1250 Ma unroofing at the Great Unconformity and <20 Ma canyon carving. *Geology* **50**, 222–226 (2022).
17. J. M. Timmons *et al.*, Tectonic inferences from the ca. 1255–1100 Ma Unkar Group and Nankoweap Formation, Grand Canyon: Intracratonic deformation and basin formation during protracted Grenville orogenesis. *Bull. Geol. Soc. Am.* **117**, 1573–1595 (2005).
18. C. Dehler *et al.*, Synthesis of the 780–740 Ma Chuar, Uinta Mountain, and Pahrump (ChUMP) groups, western USA: Implications for Laurentia-wide cratonic marine basins. *Geol. Soc. Am. Bull.* **129**, 607–624 (2017).
19. A. D. Rooney *et al.*, Coupled Re-Os and U-Pb geochronology of the Tonian Chuar Group. *Grand Canyon. Geol. Soc. Am. Bull.* **130**, 1085–1098 (2018).
20. P. F. Hoffman, Glacial erosion on a snowball earth: Testing for bias in flux balance, geographic setting, and tectonic regime. *Can. J. Earth Sci.* **60**, 765–777 (2022).
21. C. A. Partin, P. M. Sadler, Slow net sediment accumulation sets snowball Earth apart from all younger glacial episodes. *Geology* **44**, 1019–1022 (2016).
22. A. R. Tasistro-Hart, F. A. Macdonald, Phanerozoic flooding of North America and the Great Unconformity. *Proc. Natl. Acad. Sci. U.S.A.* **120**, 1–9 (2023).
23. E. S. C. Anttila, F. A. Macdonald, J. Zinto, M. D. Britt, The real McCoy: Great Unconformity source-to-sink on the rifted passive margin of Laurentia. *Earth Planet. Sci. Lett.* **642**, 118852 (2024).
24. X. Wang, X. Zhang, W. Liu, Biostratigraphic constraints on the age of Neoproterozoic glaciation in North China. *J. Asian Earth Sci.* **219**, 104894 (2021).
25. Y. Sun *et al.*, Global sea-level fall triggered Ediacaran-Cambrian unconformity in North China craton. *Earth Planet. Sci. Lett.* **622**, 118411 (2023).
26. L. Pang *et al.*, Detrital zircon U-Pb age and Hf isotopic composition and whole-rock geochemical characteristics of the Statherian Huangqikou Formation, western margin of the North China Craton: Implications for provenance and tectonic evolution. *Precambrian Res.* **347**, 105840 (2020).
27. R. N. Mitchell *et al.*, The supercontinent cycle. *Nat. Rev. Earth Environ.* **2**, 358–374 (2021).
28. G. H. Spence, D. P. Le Heron, I. J. Fairchild, Sedimentological perspectives on climatic, atmospheric and environmental change in the Neoproterozoic ear. *Sedimentology* **63**, 253–306 (2016).
29. P. F. Hoffman *et al.*, Snowball Earth climate dynamics and Cryogenian geology-geobiology. *Sci. Adv.* **3**, e1600983 (2017).

30. G. Zhao, P. A. Cawood, S. A. Wilde, M. Sun, Review of global 2.1–1.8 Ga orogens: Implications for a pre-Rodinia supercontinent. *Earth Sci. Rev.* **59**, 125–162 (2002).
31. G. Zhao, M. Sun, S. A. Wilde, S. Li, Assembly, accretion and breakup of the Paleo-mesoproterozoic Columbia supercontinent: Records in the North China Craton. *Gondwana Res.* **6**, 417–434 (2003).
32. T. M. Kusky *et al.*, Insights into the tectonic evolution of the North China Craton through comparative tectonic analysis: A record of outward growth of Precambrian continents. *Earth Sci. Rev.* **162**, 387–432 (2016).
33. B. Wan, B. F. Windley, W. Xiao, J. Feng, J. Zhang, Paleoproterozoic high-pressure metamorphism in the northern North China Craton and implications for the Nuna supercontinent. *Nat. Commun.* **6**, 8344 (2015).
34. Q. R. Meng, H. H. Wei, Y. Q. Qu, S. X. Ma, Stratigraphic and sedimentary records of the rift to drift evolution of the northern North China craton at the paleo- to mesoproterozoic transition. *Gondwana Res.* **20**, 205–218 (2011).
35. M. Zhai, B. Hu, T. Zhao, P. Peng, Q. Meng, Late Paleoproterozoic-Neoproterozoic multi-rifting events in the North China Craton and their geological significance: A study advance and review. *Tectonophysics.* **662**, 153–166 (2014).
36. J. K. Ding *et al.*, North China craton: The conjugate margin for northwestern Laurentia in Rodinia. *Geology* **49**, 773–778 (2021).
37. X. M. Fu *et al.*, New paleomagnetic results from the Huaibei Group and Neoproterozoic mafic sills in the North China Craton and their paleogeographic implications. *Precambrian Res.* **269**, 90–106 (2015).
38. H. Zhao *et al.*, New paleomagnetic results from the ca. 1.0 Ga Jiayuan Formation of the Huaibei Group in the North China craton, and their paleogeographic implications. *Precambrian Res.* **379**, 106807 (2022).
39. Z. Li *et al.*, The late Stenian and late Tonian provenance transitions in the northern Xuhuai Basin: Implications for the Precambrian evolution of the southeastern North China Craton. *J. Asian Earth Sci.* **264**, 106070 (2024).
40. M. Tan, Z. Li, Z. Lan, W. An, D. Wang, Rodinia supercontinent assembly in the southeastern North China Craton: Detrital zircon evidence from the late Ediacaran Fengtai Formation. *Precambrian Res.* **422**, 107775 (2025).
41. S. Li *et al.*, Global meso- neoproterozoic plate reconstruction and formation mechanism for Precambrian basins: Constraints from three cratons in China. *Earth-Sci. Rev.* **198**, 102946 (2019).
42. S. Zhang, Z. X. Li, H. Wu, New Precambrian palaeomagnetic constraints on the position of the North China Block in Rodinia. *Precambrian Res.* **144**, 213–238 (2006).
43. H. Peng *et al.*, Long-term and multiple stage exhumation of the Ordos Basin, western North China Craton: Insights from seismic reflection, borehole and geochronological data. *Earth-Sci. Rev.* **238**, 104349 (2023).
44. D. P. Le Heron *et al.*, Bird's-eye view of an Ediacaran subglacial landscape. *Geology* **47**, 705–709 (2019).
45. R. E. Havranek, R. M. Flowers, Zircon (U-Th)/He data for the Colorado Front Range "fourteeners" and testing Cryogenian exhumation of sub-Great Unconformity basement. *Chem. Geol.* **591**, 120702 (2022).
46. B. A. Peak, R. M. Flowers, F. A. Macdonald, Ediacaran-Ordovician tectonic and geodynamic drivers of Great Unconformity exhumation on the southern Canadian Shield. *Earth Planet. Sci. Lett.* **619**, 118334 (2023).
47. F. A. Macdonald, W. A. Yonkee, R. M. Flowers, N. L. Swanson-Hysell, Neoproterozoic of Laurentia. *Mem. Geol. Soc. Am.* **220**, 331–380 (2023).
48. K. E. Karlstrom, J. M. Timmons, L. J. Crossey, Introduction to grand canyon geology. *Spec. Pap. Geol. Soc. Am.* **489**, 1–6 (2012).
49. C. Lu *et al.*, Characterising early Precambrian collisional orgens: A metamorphic perspective from the Lüliang Complex and the Trans-North China Orogen. *Earth-Sci. Rev.* **245**, 104566 (2023).
50. K. Karlstrom *et al.*, Cambrian sauk transgression in the Grand Canyon region redefined by detrital zircons. *Nat. Geosci.* **11**, 438–443 (2018).
51. W. R. Guenthner, P. W. Reiners, H. Drake, M. Tillberg, Zircon, titanite, and apatite (U-Th)/He ages and age-eU correlations from the Fennoscandian Shield, southern Sweden. *Tectonics* **36**, 1254–1274 (2017).
52. P. Söderlund, L. M. Page, U. Söderlund, ^{40}Ar-^{39}Ar biotite and hornblende geochronology from the Oskarshamn area, SE Sweden: Discerning multiple Proterozoic tectonothermal events. *Geol. Mag.* **145**, 790–799 (2008).
53. J. K. Hourigan, P. W. Reiners, M. T. Brandon, U-Th zonation-dependent alpha-ejection in (U-Th)/He chronometry. *Geochim. Cosmochim. Acta* **69**, 3349–3365 (2005).
54. W. E. Hames, S. A. Bowring, An empirical evaluation of the argon diffusion geometry in muscovite. *Earth Planet. Sci. Lett.* **124**, 161–169 (1994).
55. U. G. Cordani, K. Sato, W. Sproessner, F. S. Fernandes, U-Pb zircon ages of rocks from the Amazonas Territory of Colombia and their bearing on the tectonic history of the NW sector of the Amazonian Craton. *Braz. J. Geol.* **46**, 5–35 (2016).
56. A. Bonilla *et al.*, The NW Amazonian craton in Guainía and Vaupes departments, Colombia: Transition between orogenic to anorogenic environments during the Paleo-Mesoproterozoic. *Precambrian Res.* **360**, 106223 (2021).
57. A. Bonilla *et al.*, The NW Amazonian Craton in Guainía and Vaupés departments, Colombia: Evidence of a Mesoproterozoic thermal event from apatite LA-ICP-MS U-Pb geochronology and its relation to continental rifting. *Precambrian Res.* **395**, 107148 (2023).
58. K. E. Karlstrom *et al.*, "Paleoproterozoic rocks of the Granite Gorges" in *Grand Canyon Geology*, S.S, M. Morales. Beus, Ed. (Oxford University Press, 2003), pp. 9–38.
59. J. McDermott, "Microstructural, geochronologic and thermochronologic evidence for both Paleo- and Mesoproterozoic displacement across the Gneiss Canyon shear zone: lower Granite Gorge, Grand Canyon, Arizona", MS thesis (University of New Mexico, Albuquerque, NM, 2011), https://digitalrepository.unm.edu/eps_etds/52/.
60. R. Rohs, Timing of thermal overprints in the Silvermines Granite and associated Diabase intrusions, St. Francois Mountains, Missouri. *Compass Earth Sci. J. Sigma Gamma Epsilon* **85**, 79–97 (2013).
61. M. E. Bickford, W. R. Van Schmus, K. E. Karlstrom, P. A. Mueller, G. D. Kamenov, Mesoproterozoic-trans-Laurentian magmatism: A synthesis of continent-wide age distributions, new SIMS U-Pb ages, zircon saturation temperatures, and Hf and Nd isotopic compositions. *Precamrian Res.* **265**, 286–312 (2015).
62. K. R. Chamberlain, S. C. Patel, B. R. Frost, G. L. Snyder, Thick-skinned deformation of the Archean Wyoming province during Proterozoic arc-continent collision. *Geology* **21**, 995–998 (1993).
63. B. R. Frost, K. R. Chamberlain, S. Swapp, C. D. Frost, T. P. Hulsebosch, Late archean structural and metamorphic history of the Wind River Range: Evidence for a long-lived active margin on the Archean Wyoming craton. *Bull. Geol. Soc. Am.* **112**, 564–578 (2000).
64. B. Wan *et al.*, Seismological evidence for the earliest global subduction network at 2 Ga ago. *Sci. Adv.* **6**, 1–9 (2020).
65. A. K. Gibbs, C.N. Barron, *The Geology of the Guyana Shield* (Clarendon Press, Oxford, 1993).
66. M. J. Jackson, D. L. Scott, D. J. Rawlings, Stratigraphic framework for the Leichhardt and Calvert superbasins: Review and correlations of the pre-1700 Ma successions between Mt Isa and McArthur River. *Aust. J. Earth Sci.* **47**, 381–403 (2000).
67. A. Davidson, Late paleoproterozoic to mid-neoproterozoic history of northern Laurentia: An overview of central Rodinia. *Precambrian Res.* **160**, 5–22 (2008).
68. K. Gallagher, Transdimensional inverse thermal history modeling for quantitative thermochronology. *J. Geophys. Res. Solid Earth.* **117**, 1–16 (2012).
69. A. Fonseca, S. Nachtergaele, A. Bonilla, S. Dewaele, J. De Grave, Extensional exhumation of cratons: Insights from the Early Cretaceous Rio Negro-Juruena belt (Amazonian Craton, Colombia). *Solid Earth* **15**, 329–352 (2024).
70. D. A. Orme, W. R. Guenthner, A. K. Laskowski, P. W. Reiners, Long-term tectonothermal history of Laramide basement from zircon–He age-eU correlations. *Earth Planet. Sci. Lett.* **453**, 119–130 (2016).
71. N. Z. Reade, J. M. Biddle, J. W. Ricketts, J. M. Amato, Zircon (U-Th)/He thermochronologic constraints on the long-term thermal evolution of Southern New Mexico and Western Texas. *Lithosphere* **2020**, 1–25 (2020).
72. X. Chen, Y. Zhou, G. A. Shields, Progress towards an improved Precambrian seawater 87Sr/86Sr curve. *Earth-Sci. Rev.* **224**, 103869 (2022).
73. J. A. Mulder, P. A. Cawood, Evaluating preservation bias in the continental growth record against the monazite archive. *Geology* **50**, 243–247 (2022).
74. C. J. Spencer *et al.*, Proterozoic onset of crustal reworking and collisional tectonics: Reappraisal of the zircon oxygen isotope record. *Geology* **42**, 451–454 (2014).
75. K. E. Sundell, F. A. Macdonald, S. J. Puetz, Does zircon geochemistry record global sediment subduction? *Geology* **52**, 282–286 (2024).
76. K. C. Condie, R. C. Aster, Refinement of the supercontinent cycle with Hf. Nd and Sr isotopes. *Geosci. Front.* **4**, 667–680 (2013).
77. D. H. Erwin *et al.*, The cambrian conundrum: Early divergence and later ecological success in the early history of animals. *Science* **334**, 1091–1097 (2011).
78. R. L. Shreve, M. Cloos, Dynamics of sediment subduction, melange formation, and prism accretion. *J. Geophys. Res. Solid Earth* **91**, 10229–10245 (1986).
79. K. E. Sundell, F. A. Macdonald, The tectonic context of hafnium isotopes in zircon. *Earth Planet. Sci. Lett.* **584**, 117426 (2022).
80. G. Shields, J. Veizer, Precambrian marine carbonate isotope database: Version 1.1. *Geochem., Geophys. Geosyst.* **3** (2002), 10.1029/2001GC000266.
81. H. L. Yuan *et al.*, Accurate U-Pb age and trace element determinations of zircon by laser ablation-inductively coupled plasma mass spectrometry. *Geostand. Geoanal. Res.* **28**, 353–370 (2004).
82. P. Vermeesch, IsoplotR: A free and open toolbox for geochronology. *Geosci. Front.* **9**, 1479–1493 (2018).
83. Z. Hu *et al.*, "Wave" signal-smoothing and mercury-removing device for laser ablation quadrupole and multiple collector ICPMS analysis: Application to lead isotope analysis. *Anal. Chem.* **87**, 1152–1157 (2015).
84. Y. S. Liu *et al.*, In situ analysis of major and trace elements of anhydrous minerals by LA-ICP-MS without applying an internal standard. *Chem. Geol.* **257**, 34–43 (2008).
85. P. Cheng, G. K. Koyanagi, D. K. Bohme, On the chemical resolution of the ^{87}Rb+ (s^{0})/^{87}Sr+ (s^{1}) isobaric interference: A kinetic search for an optimum reagent. *Anal. Chim. Acta* **627**, 148–153 (2008).
86. K. J. Hogmalm, T. Zack, A. K. Karlsson, A. S. L. Sjoqvist, D. Grabe-Schonberg, In-situ Rb-Sr and K-Ca dating by LA-ICP-MS/MS: An evaluation of N_2O and SF_6 as reaction gases. *J. Anal. At. Spectrom.* **32**, 305–313 (2017).
87. L. Gorojovsky, O. Alard, Optimisation of laser and mass spectrometer parameters for the: In situ analysis of Rb/Sr ratios by LA-ICP-MS/MS. *J. Anal. At. Spectrom.* **35**, 2322–2336 (2020).
88. C. Y. Wang *et al.*, Advances in in-situ Rb-Sr dating using LA-ICP-MS/MS: Applications to igneous rocks of all ages and to the identification of unrecognized metamorphic events. *Chem. Geol.* **610**, 121073 (2022).
89. C. Paton, J. Hellstrom, B. Paul, J. Woodhead, J. Hergt, Iolite: Freeware for the visualization and processing of mass spectrometric data. *J. Anal. At. Spectrom.* **26**, 2508–2518 (2011).
90. P. W. Reiners, T. L. Spell, S. Nicolescu, K. A. Zanetti, Zircon (U-Th)/He thermochronometry: He diffusion and comparisons with ^{40}Ar/^{39}Ar dating. *Geochim. Cosmochim. Acta* **68**, 1857–1887 (2004).
91. P. W. Reiners, Zircon (U-Th)/He thermochronometry. *Rev. Mineral. Geochemi.* **58**, 151–179 (2005).
92. J. K. Höurigan, P. W. Reiners, M. T. Brandon, U-th zonation-dependent alpha-ejection in (U-Th)/He chronometry. *Geochim. Cosmochim. Acta* **69**, 3349–3365 (2005).
93. K. Gallagher, K. Charvin, S. Nielsen, M. Sambridge, J. Stephenson, Markov chain Monte Carlo (MCMC) sampling methods to determine optimal models, model resolution and model choice for Earth Science problems. *Mar. Pet. Geol.* **26**, 525–535 (2009).
94. W. R. Guenthner, P. W. Reiners, R. A. Ketcham, L. Nasdala, G. Giester, Helium diffusion in natural zircon: Radiation damage, anisotropy, and the interpretation of zircon (U-Th)/He thermochronology. *Am. J. Sci.* **313**, 145–198 (2013).
95. A. L. Abbey, M. Wildman, A. L. S. Goddard, K. E. Murray, Thermal history modeling techniques and interpretation strategies: Applications using QTQt. *Geosphere* **19**, 493–530 (2023).
96. R. A. Ketcham, Thermal history inversion from thermochronometric data and complementary information: New methods and recommended practices. *Chem. Geol.* **653**, 122042 (2024).
97. R. M. Flowers, B. A. Peak, Context matters: Modeling thermochronologic data in geologic frameworks using the Great Unconformity as a case study. *Earth Planet. Sci. Lett.* **650**, 119061 (2025).
98. R. A. Ketcham, A. Carter, R. A. Donelick, J. Barbarand, A. J. Hurford, Improved measurement of fission-track annealing in apatite using c axis projection. *Am. Mineral.* **92**, 789–798 (2007).
99. M. G. Malusa, P. Philippot, M. Zattin, S. Martin, Late stages of exhumation constrained by structural, fluid inclusion and fission track analyses (Sesia-Lanzo unit, Western European Alps). *Earth Planet. Sci. Lett.* **243**, 565–580 (2006).
100. C. de Capitani, K. Petrakakis, The computation of equilibrium assemblage diagrams with Theriak/Domino software. *Am. Mineral.* **95**, 1006–1016 (2010).
101. T. J. B. Holland, R. Powell, An internally consistent thermodynamic data set for phases of petrological interest. *J. Metamorph. Geol.* **16**, 309–343 (1998).

102. T. J. B. Holland, R. Powell, An improved and extended internally consistent thermodynamic dataset for phases of petrological interest, involving a new equation of state for solids. *J. Metamorph. Geol.* **29**, 333–383 (2011).
103. R. W. White, R. Powell, T. J. B. Holland, T. E. Johnson, E. C. R. Green, New mineral activity–composition relations for thermodynamic calculations in metapelitic systems. *J. Metamorph. Geol.* **32**, 261–286 (2014).
104. T. J. B. Holland, R. Powell, Activity–composition relations for phases in petrological calculations: An asymmetric multicomponent formulation. *Contrib. Mineral. Petrol.* **145**, 492–501 (2003).
105. R. W. White, R. Powell, G. L. Clarke, The interpretation of reaction textures in Fe-rich metapelitic granulites of the Musgrave Block, central Australia: Constraints from mineral equilibria calculations in the system K_2O–FeO–MgO–Al_2O_3–SiO_2–H_2O–TiO_2–Fe_2O_3. *J. Metamorph. Geol.* **20**, 41–55 (2002).
106. F. J. Korhonen, R. Powell, J. H. Stout, Stability of sapphirine + quartz in the oxidized rocks of the Wilson Lake terrane, Labrador: Calculated equilibria in NCKFMASHTO. *J. Metamorph. Geol.* **30**, 21–36 (2012).
107. K. Gallagher, QTQt thermal history modeling software. Thermonet. https://www.thermonet.cnrs.fr/en/software-programs/qtqt-software/qtqt-version-and-update/. Deposited 17 June 2024.
108. C. de Captitani. Theriak-Domino phase equilibrium modelling program. Minpet. https://titan.minpet.unibas.ch/minpet/theriak/theruser.html. Accessed 8 March 2025
109. T. J. B. Holland, R. Powell, Thermocalc database ds62 for use with the Theriak-Domino suite of programs. Thermocalc. https://hpxeosandthermocalc.org/the-hpx-eos/hpx-eos-implementation/?_refluxos=a10. Accessed 8 March 2025.